Numerical simulations of capsule deformation using a dual time-stepping lattice Boltzmann method

Charles Armstrong and Yan Peng

Phys. Rev. E **103**, 023309 — Published 26 February 2021

DOI: 10.1103/PhysRevE.103.023309

NUMERICAL SIMULATIONS OF CAPSULE DEFORMATION USING A DUAL TIME-STEPPING LATTICE BOLTZMANN METHOD

CHARLES ARMSTRONG AND YAN PENG

Abstract In this work a quasi-steady, dual time-stepping lattice Boltzmann method is proposed for simulation of capsule deformation. At each time step the steady state lattice Boltzmann equation is solved using the full approximation storage multigrid scheme for non-linear equations. The capsule membrane is modeled as an infinitely thin shell suspended in an ambient fluid domain with the fluid structure interaction computed using the Immersed Boundary Method. A finite element method is used to compute the elastic forces exerted by the capsule membrane. Results for a wide range of parameters and initial configurations are presented. The proposed method is found to reduce the computational time by a factor of ten.

1. Introduction

Capsules are elastic, fluid-filled membranes enclosing a Newtonian fluid, which serve as a useful model for biological and synthetic membranes. One prominent application of capsules has been to model the material properties of red blood cells. A number of experiments have been conducted on suspensions of red blood cells in a shear flow (e.g. [1, 2, 3, 4]). As such, shear-induced capsule deformation has been the subject of extensive mathematical modeling.

Early analytical work was conducted by Barthés-Biesel [5] and Barthés-Biesel and Rallison [6] who used perturbation theory to predict the deformation of spherical capsules in shear flow in the limit of small deformations. Keller and Skalak [7] studied the behavior of rigid two dimensional ellipsoids in shear flow. This work was later extended to ellipsoids with elastic [8] and viscoelastic [9] membranes.

Because of the complex dynamics associated with capsule deformation, numerical studies have also drawn interest from researchers. Early numerical studies include the boundary element method (BEM) simulations done by Pozrikidis [10, 11] and Ramanujan and Pozrikidis [12] and the three dimensional Immersed Boundary Method (IBM) [13] simulations reported by Eggleton and Popel in [14]. As computing power has progressed the body of research on capsule simulations of red blood cells has grown considerably, including BEM simulations in [15, 16, 17, 18, 19, 20] and front-tracking and IBM simulations in [21, 22, 23, 24, 25, 26, 27, 28].

In this work we propose a quasi-steady, dual time-stepping (DTS) scheme that couples the multigrid lattice Boltzmann method (LBM) [29] to a IBM method in

order to reduce the computational time required to simulate flow-induced capsule deformation at low Reynolds numbers. The fluid structure algorithm used here is similar to the LBM-IBM implementations discussed in [22, 30, 31]. The elasticity of the membrane is modeled using the finite element method proposed by Charrier et al. in [32], where a constitutive law determines the membrane response to in-plane tensions. The capsule's bending resistance is described by the Helfrich bending functional [33, 34] and viscosity jumps across the membrane surface are handled using the front-tracking method proposed by Zhang et al. in [35].

For LBM-IBM simulations of capsule deformation the resolution of the fluid velocity plays an outsized role in the accuracy of the method [30]. Because of this, a relatively fine Eulerian mesh is desirable. Due to the coupling between the temporal and spatial discretizations of the lattice Boltzmann equation this places a stringent constraint on the time step. For LBM-IBM simulations this limitation results in a time step that is orders of magnitude smaller than the elastic and fluid time scales of the problem.

The large separation between the relevant temporal and spatial scales suggests that de-coupling the LBM time step from the physical time step by employing a DTS scheme could reduce the computational time required for capsule simulations. Applications of DTS have been reported for spectral [36] and finite volume [37] models of the lattice Boltzmann equation. More recently a DTS procedure was incorporated into a LBM-IBM scheme for simulation of flow past a cylinder [38]. The transient terms were added as a source into the LBE, and the resulting equations are solved using the multigrid lattice Boltzmann method originally developed by Mavriplis in [29]. The authors reported speed up of approximately 4 when compared with the traditional LBM for unsteady flow past a cylinder [38].

In this work we propose a quasi-steady implementation of the LBM-IBM capsule model, treating each time step as a steady flow problem. This allows us to de-couple the LBM time discretization, which is tied to the spatial discretization, from the capsule discretization. This allows for a physical time step orders of magnitude larger than the one required by traditional LBM-IBM capsule models. Neglecting the transient terms of the incompressible Navier-Stokes equations reduces the computational and memory requirements when compared with the method proposed in [38] without sacrificing accuracy in the low Reynolds number regime of capsule deformation. The proposed quasi-steady scheme also allows for easy incorporation into pre-existing LBM-IBM capsule codes, offering efficiency gains of one order of magnitude with the newly proposed scheme.

The structure of this paper is as follows: Section 2 discusses the physical model of capsule deformation in shear flow. Section 3 discusses the multigrid lattice Boltzmann method. Section 4 presents the methods used for computation of the capsule forces. Section 5 discusses the fluid-structure interaction algorithm. Section 6 discusses the coupling of the multigrid LBM to the capsule model. Section 7 presents the results from the capsule model for a variety of capsule geometries

and parameters. Section 8 discusses the efficiency gains resulting from the multi-grid DTS implementation. Section 9 concludes the paper with a discussion of the validity and applicability of the quasi-steady scheme proposed here.

2. Problem Description

In this work we simulate the flow-induced deformation of a capsule in shear flow. The capsule membrane is modeled as a two-dimensional, fluid-filled, elastic membrane surrounded by an ambient fluid. The plane of shear is the x-y plane, with periodic boundaries in the z coordinate direction. The capsule is initially inclined by $\pi/4$ radians with respect to the x axis.

A schematic illustration of the plane of shear can be seen in Figure 1. The shear rate for the flow is $[k] = \mathrm{s}^{-1}$. The ambient fluid has viscosity, $[\mu_a] = \mathrm{Pa} \cdot \mathrm{s}$, and the interior fluid has viscosity $[\mu_c] = \mathrm{Pa} \cdot \mathrm{s}$. The capsule size is parametrized by the equivalent radius, $[a] = \mathrm{m}$, defined as the radius of a sphere with the same volume as the capsule. The elasticity of the capsule is parametrized by the Young's surface modulus, $[E_s] = \mathrm{N} \cdot \mathrm{m}^{-1}$, and the capsule's bending resistance is parametrized by the bending stiffness modulus, $[E_B] = \mathrm{J}$.

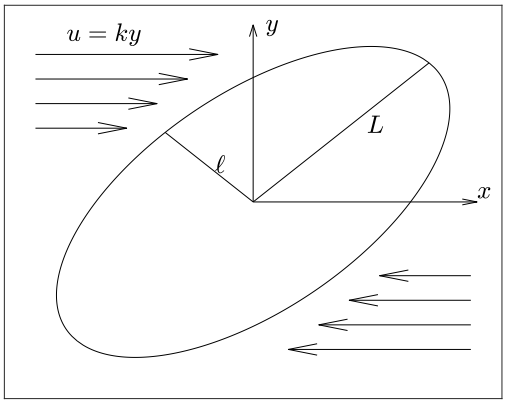

Figure 1. The initial configuration for a spheroidal capsule in shear flow.

These parameters can be combined into a number of dimensionless parameters that characterize the dynamics of shear-induced capsule deformation. The capillary number, also referred to as the dimensionless shear rate by some researchers, is the ratio of the viscous to elastic forces and is given by:

$$\mathrm{Ca} = \frac{\mu_a a k}{E_s}. \tag{1}$$

The dimensionless bending stiffness is the ratio of the bending forces to the elastic forces and is given by:

$$E_b = \frac{E_B}{a^2 E_s}. \tag{2}$$

The viscosity ratio is the ratio of the internal capsule viscosity, μ_c, to the ambient fluid viscosity, μ_a:

$$V = \frac{\mu_c}{\mu_a}. \tag{3}$$

For numerical studies typical ranges of these parameters are as follows: Ca $= 0.01 - 1$, $V = 0.1 - 10$, and $E_b = 0 - 0.1$.

For shear-induced capsule deformation the Reynolds number is given by:

$$\mathrm{Re} = \frac{\rho k a^2}{\mu_a}. \tag{4}$$

For biological and microcapsule applications $\mathrm{Re} \ll 1$ [3, 4, 39, 40] and thus, numerical studies often use the Stokes approximation [12, 15, 16, 41]. Numerical studies that do consider the fluid inertia use Reynolds numbers in the range of $\mathrm{Re} = 0.01 - 0.1$ [21, 22, 26, 30, 31, 42].

The capsule dynamics are analyzed by looking at the the deformation parameter, D_{xy}, and the inclination angle, θ. Initially proposed by Taylor in [43], the deformation parameter of a two dimensional capsule is computed from the lengths of the major and minor axes (denoted by L and ℓ respectively in Figure 1) of the capsule as follows:

$$D_{xy} = \frac{L - \ell}{L + \ell}. \tag{5}$$

The inclination angle is the angle between the capsule's major axis and the x coordinate axis.

For spherical capsules at moderate capillary numbers ($\mathrm{Ca} \lesssim 0.2$) the capsule will deform until reaching an approximately constant equilibrium shape [5, 6]. After reaching a constant shape, the flow causes the membrane to rotate around the internal fluid without further deformation. This phenomenon, known as tank-treading, has also been observed experimentally for spherical [40] and biconcave [1] capsules.

The dynamics of capsules with non-spherical geometries and capsules at larger values of Ca exhibit a wide variety of behaviors [4, 8, 9, 40]. In general, higher values of Ca result in more deformation and greater rotation of the capsule toward the x-axis. For large values of Ca, capsule breakup will occur [39]. For non-spherical capsules the dynamics typically do not reach a steady deformed shape or orientation, and instead orientation and deformation will exhibit oscillatory or intermittent behavior [3, 8].

3. Fluid Solver

The fluid motion inside and outside the capsule is governed by the incompressible Navier-Stokes equations:

$$\rho(\partial_t \mathbf{u} + \mathbf{u} \cdot \nabla \mathbf{u}) = -\nabla p + \mu \nabla^2 \mathbf{u} + \mathbf{p} \tag{6}$$

$$\nabla \cdot \mathbf{u} = \mathbf{0} \tag{7}$$

where ρ is the fluid density, $\mathbf{u}$ is the fluid velocity, μ is the fluid viscosity, p is the pressure and $\mathbf{p}$ is the external force.

As discussed above, the typical Reynolds number for numerical simulations of capsule deformation are on the order of 10^{-2}, and thus the inertial terms in the Navier-Stokes equations have only a small effect on the flow field. Due to this observation, we neglect the transient term in Equation (6) and instead solve the steady-state system:

$$\rho \mathbf{u} \cdot \nabla \mathbf{u} = -\nabla p + \mu \nabla^2 \mathbf{u} + \mathbf{p} \tag{8}$$

$$\nabla \cdot \mathbf{u} = \mathbf{0} \tag{9}$$

at each time step. This allows us to de-couple the LBM discretization from the temporal discretization. Furthermore, treating the fluid computation at each time step as a steady flow, we can use the multigrid lattice Boltzmann method proposed in [29] to accelerate the fluid computation.

3.1. The lattice Boltzmann Method.

In this work we solve Equations (8) and (9) using the lattice Boltzmann method (LBM). In LBM the fluid is modeled as a system of discrete particles whose distribution function evolves based on the lattice Boltzmann equation (LBE) given by:

$$f_i(\mathbf{x} + \mathbf{c}_i \delta t, t + \delta t) - f_i(\mathbf{x}, t) = \Omega_i(f), \ i = 0, 1, \ldots, N \tag{10}$$

where Ω describes the collisions between particles, h is the spatial step, δt is the time step, $N + 1$ is the number of discrete velocities in the model, $\mathbf{c}_i$ is the i^{th} discrete velocity, and f_i is the distribution function associated with the i^{th} velocity.

The discretization of space, time, and velocity in the LBE are inter-related as follows:

$$\delta t = \frac{\Delta x}{c} \qquad \mathbf{c}_i = c\ \mathbf{e}_i \qquad c_s = \frac{1}{\sqrt{3}} c \tag{11}$$

where c_s is the speed of sound in the material and c is dependent on the lattice. For the D3Q19 discretization used here, the values of $\mathbf{e}_i$ are given as:

(12)

$$[\mathbf{e}_0, \mathbf{e}_1, \mathbf{e}_2, \ldots, \mathbf{e}_{18}] = \begin{bmatrix} 0 & 1 & -1 & 0 & 0 & 0 & 0 & 1 & 1 & -1 & -1 & 1 & -1 & 1 & -1 & 0 & 0 & 0 & 0 \\ 0 & 0 & 0 & 1 & -1 & 0 & 0 & 1 & -1 & 1 & -1 & 0 & 0 & 0 & 0 & 1 & 1 & -1 & -1 \\ 0 & 0 & 0 & 0 & 0 & 1 & -1 & 0 & 0 & 0 & 0 & 1 & 1 & -1 & -1 & 1 & -1 & 1 & -1 \end{bmatrix}.$$

For the above $\mathbf{e_i}$, a choice of $c = 1$ m/s results in the particle distribution functions moving exactly one grid point at each time step, eliminating the need for interpolation.

In this work, the collision term, Ω, in Equation (10) is approximated using the multiple relaxation time (MRT) collision model discussed in [44]. The MRT collision operator maps the distribution function to the physical moments of the system where each moment is relaxed to its corresponding equilibrium moment. With the above discretization, the MRT collision model can be implemented in the following two-step procedure:

$$\begin{aligned} &\text{Collision: } f_i^*(\mathbf{x}) = f_i(\mathbf{x}, t_n) - M_{ij}^{-1} S_{jk}[M_{kl} f_l(\mathbf{x}, t_n) - m_k^{eq}(\mathbf{x}, t_n)] \\ &\text{Advection: } f_i(\mathbf{x} + \mathbf{c}_i \delta t, t_n + \delta t) = f_i^*(\mathbf{x}),\ i = 0, 1, \ldots, 18\ . \end{aligned} \tag{13}$$

Here m_k^{eq} is the k^{th} equilibrium moment, S_{jk} are the components of the relaxation matrix, $\mathbf{S}$, and M_{jk} are the components of the collision matrix mapping f to the moment space. $\mathbf{m}^{eq}$ and the collision matrix, $\mathbf{M}$, are the same as derived in [44].

The relaxation matrix, $\mathbf{S}$, is defined as:

$$\mathbf{S} = \text{diag}(s_0, s_1, s_2, s_3, s_4, s_5, s_6, s_7, s_8, s_9, s_{10}, s_{11}, s_{12}, s_{13}, s_{14}, s_{15}, s_{16}, s_{17}, s_{18}). \tag{14}$$

s_0, s_3, s_5, and s_7 correspond to the conserved moments and hence are set equal to zero. The parameters $s_4 = s_6 = s_8 = s_9 = s_{11} = s_{13} = s_{14} = s_{15}$ are related to the kinematic viscosity, ν, as follows:

$$\nu = c_s^2 \delta t \left(\frac{1}{s_4} - \frac{1}{2} \right). \tag{15}$$

s_1 is related to the bulk viscosity, ξ, by:

$$\xi = \frac{2}{3} c_s^2 \delta t \left(\frac{1}{s_1} - \frac{1}{2} \right). \tag{16}$$

The parameters, s_2, s_{10}, s_{12}, s_{16}, s_{17}, s_{18} correspond to higher order moments that do not affect the solutions in the hydrodynamic regime and are thus set to 1.8 [44].

Once the distribution function has been updated we can compute the macroscopic variables associated with Equations (8) and (9) by computing moments of the distribution function as follows:

$$\rho = \sum_{i=0}^{N} f_i \qquad\qquad \mathbf{j} = \rho \mathbf{u} = \sum_{i=0}^{N} f_i \mathbf{c}_i\ . \tag{17}$$

Additional macroscopic variables can be obtained by computing higher order moments of the distribution function and are defined by the rows of matrix $\mathbf{M}$ [44].

To incorporate the forces, $\mathbf{p}(\mathbf{x})$, into the LBM we follow the method described in [45]. First, the momentum computed using Equation (17) is updated as follows:

$$\mathbf{j}'(\mathbf{x}) = \mathbf{j}(\mathbf{x}) + \frac{\delta t}{2} \mathbf{p}(\mathbf{x})\ . \tag{18}$$

Next, $\mathbf{j}'$ is used to compute the equilibrium moments, $\mathbf{m}^{eq}$, in Equation (13). After computing the equilibrium moments, the momentum is updated once more using:

$$\mathbf{j}''(\mathbf{x}) = \mathbf{j}'(\mathbf{x}) + \frac{\delta t}{2}\mathbf{p}(\mathbf{x}) \tag{19}$$

Finally, $\mathbf{j}''$ is used to update the moments corresponding to the fluid momentum, m_3, m_5, and m_7.

3.2. **The Multigrid Lattice Boltzmann Method.** For steady flows the LBM becomes an iterative procedure. Due to the improved error damping properties of relaxation schemes, Mavriplis [29] introduced a relaxation step following the collision and advection stages of the LBM, resulting in an iterative method analogous to the Jacobi under-relaxation scheme for linear systems. On the fine grid the Jacobi under-relaxation scheme is carried out in the following three-step procedure:

$$\begin{aligned} &\text{Collision: } f_i^*(\mathbf{x}) = f_i^n(\mathbf{x}) - M_{ij}^{-1} S_{jk}[M_{kl} f_l(\mathbf{x}) - m_k^{eq}(\mathbf{x})] \\ &\text{Advection: } f_i^{**}(\mathbf{x} + \mathbf{e}_i \Delta x) = f_i^*(\mathbf{x}),\ i = 0, 1, \ldots, 18 \\ &\text{Relaxation: } f_i^{n+1}(\mathbf{x}) = \gamma f_i^{**}(\mathbf{x}) + (1-\gamma) f_i^n(\mathbf{x}) \end{aligned} \tag{20}$$

where γ is a relaxation parameter such that $0 < \gamma < 1$.

A key component of multigrid schemes is the residual, which is used to estimate the error of the iterative solution. For the LBE the i^{th} component of the residual is given by:

$$r_i(\mathbf{f}) = f_i(\mathbf{x}) - f_i(\mathbf{x} - \mathbf{e}_i \Delta x) + M_{ij}^{-1} S_{jk} \left[M_{kl} f_l(\mathbf{x} - \mathbf{e}_i \Delta x) - m_k^{eq}(\mathbf{x} - \mathbf{e}_i \Delta x) \right] \tag{21}$$

where $\mathbf{f} \coloneqq [f_0, f_2, ..., f_{18}]^T$. On the fine grid the error equation is given by:

$$r_i^h(\mathbf{f}_h) = 0. \tag{22}$$

After solving this system for $\mathbf{f}_h$, we approximate the error by computing the residual using Equation (21). We then use point-wise injection to map the distribution function to the coarse grid and an averaging operator to map the error to the coarse grid.

On the coarse grid levels, the correction equation is written as:

$$r_i^H(\mathbf{f}_H) = D_i^H \tag{23}$$

$$D_i^H = r_i^H(\hat{I}_h^H \mathbf{f}_h) - 2 I_h^H r_i^h(\mathbf{f}_h) \tag{24}$$

where r_i^H is computed using Equation (21) and D_i^H is known as the defect correction. The factor of 2 in the second term on the right side of Equation (24) is used to scale the relaxation parameters on the coarse grids [29]. Equation (23) is solved for $\mathbf{f}_H$ in almost the same manner as Equation (20), with a modification to the relaxation step so that D_i^H can be added to the distribution function as follows:

$$\text{Relaxation: } f_i^{n+1}(\mathbf{x}) = \gamma \left[f_i^{**}(\mathbf{x}) + D_i^H(\mathbf{x}) \right] + (1-\gamma) f_i^n(\mathbf{x}). \tag{25}$$

After solving for the error on the coarse grid, the error is mapped back to the fine grid using an averaging operator and is added to our approximation of the distribution function.

3.3. **Selecting the Relaxation Parameter.** In order to determine the optimal value of γ in Equation (20) we conduct a simulation similar to the two-dimensional study conducted by Patil et al. in [46]. Simulations are conducted for three-dimensional lid driven cavity flow with the primary Reynolds number used in this paper, $\mathrm{Re} = 0.05$. In this work the fluid velocity is assumed to have converged to the correct velocity field when the following constraint has been met:

$$\frac{\sum_i |\mathbf{u}^{n+1}(\mathbf{x}_i) - \mathbf{u}^n(\mathbf{x}_i)|_2}{\sum_i |\mathbf{u}^{n+1}(\mathbf{x}_i)|_2} \leq \epsilon. \tag{26}$$

In Equation (26) ϵ is a user-defined tolerance and $|\cdot|_2$ is the L^2 norm.

For each simulation the number of multigrid cycles needed to reach a tolerance of $\epsilon = 10^{-5}$ and $\epsilon = 10^{-8}$ is recorded. The domain of the simulations is $[0,1]^3$, with a discretization of $N = 129$ nodes in each direction. The w-cycle multigrid schedule was used for these tests.

In Figure 2 the number of multigrid cycles required to reach convergence for values of γ ranging from 0.1 to 0.9 is shown. The trend for both values of ϵ is the same: increasing γ results in faster convergence until reaching a minimum between 0.8 and 0.9. Based on this, we have set $\gamma = 0.8$ for the simulations presented below.

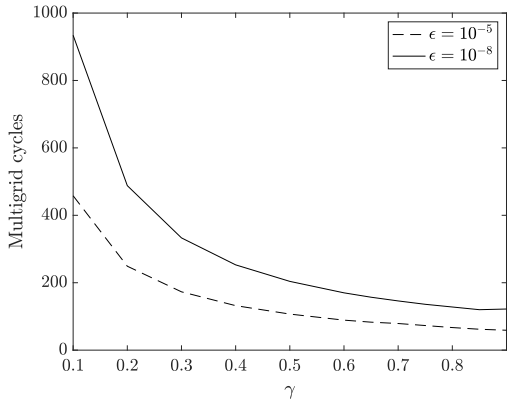

FIGURE 2. The number of multigrid iterations for solution of lid-driven cavity flow using the multigrid lattice Boltzmann method for various values of the relaxation parameter, γ.

4. Capsule Model

The capsule membrane is modeled as a two dimensional surface with transverse forces caused by in-plane tensions and normal forces caused by the capsule's

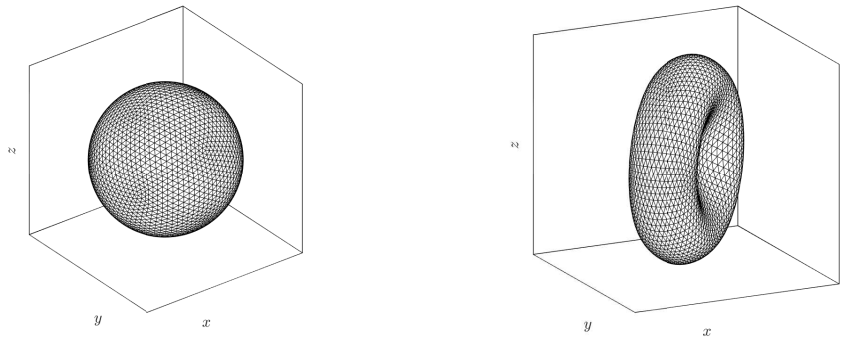

(a) (b)

FIGURE 3. (a) The spherical and (b) biconcave meshes used in this work. These discretizations have 5120 triangles composed of 2562 Lagrangian nodes.

bending resistance. The membrane discretization is a triangular mesh where each triangle's vertices are tracked as Lagrangian nodes. The positions of the vertices are advected based on the fluid velocity near the capsule membrane using the Immersed Boundary Method [13]. In this work we consider three capsule geometries: spherical, spheroidal and biconcave discoid. The mesh used for the spherical and biconcave capsules can be seen in Figures 3(a) and 3(b) respectively.

4.1. **Elastic Forces.** The elasticity of the capsule is modeled by a constitutive law describing the strain energy of the membrane. In this work we use two strain energy functions: the Neo-Hookean law and Skalak's law. The Neo-Hookean law was originally developed for three-dimensional solids, and is a function of the three dimensional principle stretches, λ_1, λ_2, and λ_3. By assuming volume incompressibility, $\lambda_1\lambda_2\lambda_3 = 1$, we can write the strain energy function in terms of λ_1 and λ_2 in the following form:

$$W^{NH} = \frac{E_s}{6}\Big[\lambda_1^2 + \lambda_2^2 + \lambda_1^{-2}\lambda_2^{-2} - 3\Big]. \tag{27}$$

The second strain energy function used in this work is Skalak's law. Proposed by Skalak et al. in [47], Skalak's law is a two-dimensional constitutive law developed to account for the resistance to surface area dilation exhibited by red blood cell membranes. The strain energy function for Skalak's law is given by:

$$W^{SK} = \frac{E_s}{8}\Big[(\lambda_1^2 + \lambda_2^2 - 2)^2 + 2(\lambda_1^2 + \lambda_2^2 - 2) - 2(\lambda_1^2\lambda_2^2 - 1) + C(\lambda_1^2\lambda_2^2 - 1)^2\Big] \tag{28}$$

The final term on the right hand side of Equation (28) can be used to approximate area incompressibility by selecting $C \gg 1$. Although Skalak's law was designed to

capture the area-incompressible red blood cell membrane, for values of $C \sim \mathcal{O}(1)$ the law can be used to simulate a general elastic membrane [41, 48].

It should be noted that there are multiple definitions of the surface elasticity modulus in the literature, varying by a constant scalar. For the Neo-Hookean law we follow the definition used in [12, 22], which results in $E_s = 3G_{nh}$, where G_{nh} is the Neo-Hookean elasticity modulus used in [48]. For Skalak's Law we follow the definition used in [22, 26], which results in $E_s = 2G_{sk}$, where G_{sk} is the Skalak elasticity modulus used in [48]. Care should be taken when comparing results from different researchers as the capillary number, Ca, Skalak parameter, C, and dimensionless bending modulus, E_b, all depend on the definition of the surface elasticity modulus that is used.

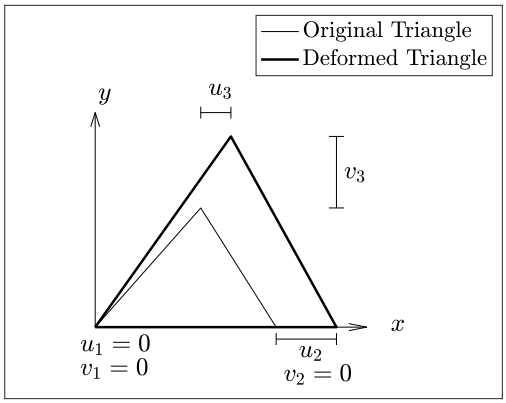

FIGURE 4. Computation of the deformation is done by mapping both triangles to a common plane.

With a constitutive law chosen, the capsule's elastic forces are computed using the linear finite element method originally proposed by Charrier et al. in [32]. First, each deformed triangular element is mapped into a common plane with its initial configuration, whereby the displacement vector, $[u, v]^T$, can be easily computed at each vertex of the triangle. The displacement vector is then fitted to a linear shape function, allowing for the computation of the right Cauchy-Green tensor and its eigenvalues, the principle stretch ratios, λ_1 and λ_2.

With u^k, v^k, λ_1, and λ_2 known we can use the principle of virtual work to obtain the following relation for the in-plane forces at the k-th vertex of the triangle:

$$\begin{aligned} P_x^k &= V_e \frac{\partial W}{\partial \lambda_1}\frac{\partial \lambda_1}{\partial u^k} + V_e \frac{\partial W}{\partial \lambda_2}\frac{\partial \lambda_2}{\partial u^k} \\ P_y^k &= V_e \frac{\partial W}{\partial \lambda_1}\frac{\partial \lambda_1}{\partial v^k} + V_e \frac{\partial W}{\partial \lambda_2}\frac{\partial \lambda_2}{\partial v^k}. \end{aligned} \tag{29}$$

Here W is the strain energy function given by either Equation (27) or Equation (28) and V_e is the element area in the undeformed state. The forces at each

vertex are then mapped back to the physical coordinates and added to the node's Lagrangian force term. For a mesh with 5120 triangles, each node is the vertex of 5 or 6 triangles. The full elastic force at a given Lagrangian node, $\mathbf{P_e}$, is the sum of the forces at each of these 5 or 6 triangles.

4.2. **Bending Forces.** The capsule's bending resistance is modeled using the shape energy functional proposed by Helfrich in [33]:

$$W_b = \frac{E_B}{2}\int_S (2\kappa - c_0)^2 dS \tag{30}$$

where κ is the mean curvature, c_0 is the spontaneous curvature and E_B is the bending stiffness modulus of the capsule. The spontaneous curvature is a parameter that defines the reference configuration for the capsule's bending energy.

The bending force density, $\mathbf{f_b}$, is obtained by taking the first variation of Equation (30), which we can express in terms of the mean curvature, κ, spontaneous curvature, c_0, and Gaussian curvature, κ_g as follows [34]:

$$\mathbf{f_b} = E_B[(2\kappa + c_0)(2\kappa^2 - 2\kappa_g - c_0\kappa) + 2\nabla_{LB}\kappa]\mathbf{n} \tag{31}$$

where ∇_{LB} is the Laplace-Beltrami operator. The nodal bending force, $\mathbf{P_b}$, is obtained from Equation (31) by multiplying $\mathbf{f_b}$ by a given node's Voroni area, A_{vor} [49].

Computation of the various terms in Equation (31) has been the subject of reviews by Guckenberg et al. in [49, 50]. In this work we compute the curvatures in Equation (31) using the method proposed by Garimella and Swartz [51], where, at each node, a quadratic surface is fitted to the node and its nearest neighbors. The mean and Gaussian curvatures, as well as the normal vector, of the Lagrangian nodes, can then be approximated from their analytical expressions using the standard formulas for an implicit surface [51].

The only term in Equation (31) remaining to be calculated is the Laplace-Beltrami of the mean curvature, $\Delta_{LB}\kappa$. Here we use the cotan Laplacian outlined in the review by Reuter et al. [52]:

$$\nabla_{LB}\kappa(\mathbf{X}_i) = \frac{1}{2A_{vor}}\sum_{j\in N(\mathbf{X}_i)} (\cot\alpha_{ij} + \cot\beta_{ij})\,[\kappa(\mathbf{X}_i) - \kappa(\mathbf{X}_j)] \tag{32}$$

where α_{ij} and β_{ij} are the exterior angles of the two triangles containing the edge created by X_j and X_i [53]. Consistent with the notation above, A_{vor} is the area of the Voroni region.

5. Fluid-Structure Interaction

5.1. **Immersed Boundary Method.** The interaction between the membrane and surrounding fluid is computed using the Immersed Boundary Method (IBM). Developed by Charles Peskin and reviewed in [13], in IBM the capsule is modeled as a set of Lagrangian coordinates suspended in a fluid-filled domain described

using Eulerian coordinates. The computation of the Lagrangian fluid velocity, $\mathbf{U}$, from the Eulerian flow velocity, $\mathbf{u}$, and the Eulerian external force, $\mathbf{p}$, from the Lagrangian forces, $\mathbf{P}$, are achieved through the following integrals:

$$\mathbf{U}(\mathbf{X}_c) = \int_V \mathbf{u}(\mathbf{x}_j)\delta(\mathbf{X}_c - \mathbf{x}_j)\ \mathrm{d}\mathbf{x}, \tag{33}$$

$$\mathbf{p}(\mathbf{x}_j) = \int_S \mathbf{P}(\mathbf{X}_c)\delta(\mathbf{X}_c - \mathbf{x}_j)\ \mathrm{d}\mathbf{X}\ . \tag{34}$$

The Lagrangian force, $\mathbf{P}$, in Equation (34) is given by $\mathbf{P} = -\mathbf{P_b} - \mathbf{P_e}$, where $\mathbf{P_b}$ and $\mathbf{P_e}$ are the bending and elastic forces at a given node. The negative signs reflect the fact that the forces are exerted by the capsule on the fluid [49].

In this work, the integrals in Equations (33) and (34) are approximated numerically using the following discrete delta function:

$$\delta_h(x) = \begin{cases} \frac{1}{4\Delta x}[1 + \cos\frac{\pi x}{2\Delta x}] & |x| \leq 2\Delta x \\ 0 & |x| > 2\Delta x\ . \end{cases} \tag{35}$$

With this approximation and the convention that $\delta_h(\mathbf{X}) = \delta_h(x)\delta_h(y)\delta_h(z)$, the computation of the integrals in Equations (33) and (34) can be written as:

$$\begin{aligned} \mathbf{U}(\mathbf{X}_c) &= \sum \mathbf{u}(\mathbf{x}_j)\delta_h(\mathbf{X}_c - \mathbf{x}_j)\Delta x^3 \\ \mathbf{p}(\mathbf{x}_j) &= \sum \mathbf{P}(\mathbf{X}_c)\delta_h(\mathbf{X}_c - \mathbf{x}_j)\Delta x^2\ . \end{aligned} \tag{36}$$

The forces, $\mathbf{p}$, computed above are then incorporated into the LBM model through Equations (18) and (19), which give us the moments of the distribution function used to compute the Eulerian fluid velocity as described above in Section 3.

Once the Lagrangian velocity has been obtained we can update the capsule's position through numerical integration of the following equation:

$$\frac{\partial \mathbf{X}_c}{\partial t} = \mathbf{U}(\mathbf{X}_c, t)\ . \tag{37}$$

In this work we use 2^{nd} order Adams-Bashforth to integrate Equation (37), giving us the following formula for updating the capsule nodes:

$$\mathbf{X}_c(t_{n+1}) = \mathbf{X}_c(t_n) + \frac{\Delta t}{2}\Big[3\mathbf{U}(\mathbf{X}_c, t_{n+1}) - \mathbf{U}(\mathbf{X}_c, t_n)\Big]\ . \tag{38}$$

Note that in our multigrid implementation, Δt is not the same value as δt, the time step in the lattice Boltzmann equation. In fact, as discussed below, values of Δt several orders of magnitude larger than δt are sufficient to produce physically accurate results using the multigrid implementation outlined in Section 6.

For explicit numerical integration of the capsule position, such as the scheme proposed here, the stability of the algorithm is given as follows [54, 55, 56]:

$$\Delta t < \alpha \frac{\mathrm{Ca} \cdot h}{ka} \tag{39}$$

where h is the size of the mesh elements and α is a constant that depends on the method of integration used to solve Equation (37).

5.2. **Fluid Viscosity.** When there is a jump between the viscosity inside the capsule, μ_c, and the viscosity of the ambient fluid, μ_a, we use the front-tracking method originally proposed by Zhang et al. in [35] for LBM-IBM models. A smoothed Heaviside function is used to compute the viscosity at points near the capsule membrane as follows:

$$\mu(\mathbf{x}) = \mu_c + (\mu_a - \mu_c)H[d(\mathbf{x})] \tag{40}$$

where $d(\mathbf{x})$ is the minimum distance between a given Eulerian point, $\mathbf{x}$, and the capsule membrane.

As in [35], the following continuous approximation to the Heaviside function in Equation (40) is used in this work:

$$H(d) = \begin{cases} 0 & d < -2\Delta x \\ \frac{1}{2}(1 + \frac{d}{2\Delta x} + \frac{1}{\pi}\sin\frac{\pi d}{2\Delta x}) & -2\Delta x \leq d \leq 2\Delta x \\ 1 & d > 2\Delta x \end{cases} \tag{41}$$

With the viscosity updated we can use $\mu(\mathbf{x})$ in Equation (15) to update the corresponding relaxation parameters associated with the LBM.

6. Multigrid Implementation

In order to demonstrate the potential for speed-up offered a dual time-stepping (DTS) scheme, we first estimate the physical time scales of the problem using k, μ_a, E_s, E_b, and a. The fluid time scale is given by $\tau_f = k^{-1}$, the elastic time scale is given by $\tau_e = \mu_a a/E_s = \mathrm{Ca}k^{-1}$ and, when bending stiffness is considered, the bending modulus time scale is given by $\tau_b = \mu_a a/(E_b E_s) = \mathrm{Ca}k^{-1}/E_b$. Since typical parameter ranges are given by $\mathrm{Ca} \sim 10^{-2} - 1$ and $E_b \sim 10^{-3} - 10^{-1}$, τ_e is the most restrictive time scale.

To illustrate the limitations of the standard LBM-IBM time step we consider the ratio of τ_e to the LBM time step:

$$\frac{\tau_e}{\delta t} = \frac{\mathrm{Ca}}{k\delta t}. \tag{42}$$

In the LBM-IBM capsule model, δt is determined by the grid resolution based on Equation (11), and thus, for a fixed value of Ca and a fixed grid resolution, $\tau_e/\delta t$ can only be adjusted by the shear rate, k. The shear rate is restricted by the stability constraint given by Equation (39). In this work we find that a shear rate, k, on the order of 10^{-4} s^{-1} is required for numerical stability. Inserting $k = 10^{-4}$ s^{-1} and the time step determined by the Eulerian grid resolution, $\delta t = 0.1$ s, the ratio into Equation (42) results in $\tau_e/\delta t \sim 10^5 \cdot \mathrm{Ca}$. The large value of $\tau_e/\delta t$ indicates that there is a large separation between the physical and LBM time scales of the problem.

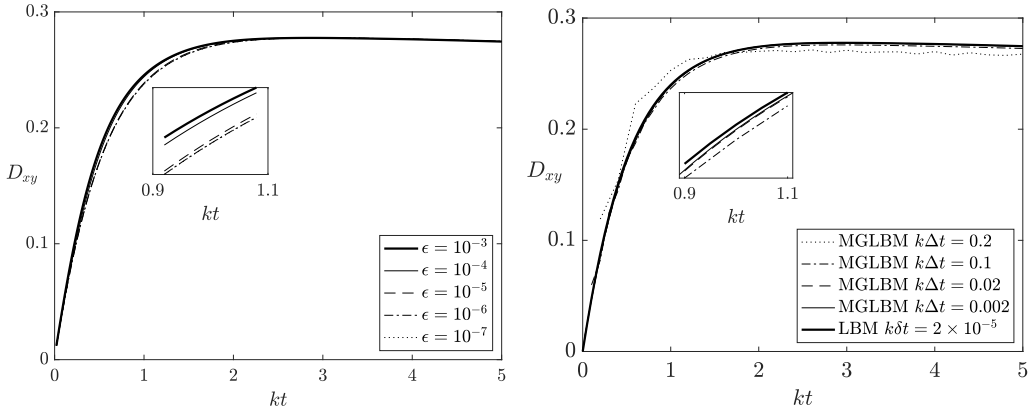

FIGURE 5. (a) D_{xy} for various choices of the iterative tolerance, ϵ. (b) D_{xy} for various time steps, Δt.

In order to de-couple the physical time step from the LBM algorithm we propose a quasi-steady, DTS LBM scheme. At each physical time step, computation of the fluid velocity is treated as a steady state problem, which is solved iteratively using the multigrid lattice Boltzmann method [29, 46, 57]. The LBM time step, δt, defined in Equation (11) becomes a pseudo-time step related to the iterative LB scheme. This allows us to introduce a new physical time step, Δt, used to update the capsule position in Equation (38), which can be adjusted without compromising the lattice structure of the LBM discretization.

6.1. **Convergence Criterion.** For iterative solution of the fluid velocity a proper choice of ϵ in Equation (26) is essential to obtaining the correct flow. In Figure 5(a) the deformation parameter, D_{xy}, is shown for values of ϵ ranging from 10^{-3} to 10^{-7} for simulations of an initially spherical capsule with Ca = 0.05, $V = 1$, $E_b = 0$, $k = 2 \times 10^{-4}$ s^{-1}, and $k\Delta t = 0.02$. As can be seen in the figure, the deformation converges to the correct final deformation for all of the values shown, however, the intermediate dynamics show slight deviations for larger tolerances, ϵ. For $\epsilon = 10^{-3}$ and $\epsilon = 10^{-4}$ the deformation occurs at a slightly faster pace, however, the curves for $\epsilon \leq 10^{-5}$ are all nearly identical.

This is best seen in the inset of Figure 5(a), which shows the differences between the values of D_{xy} between $kt = 0.9$ and $kt = 1.1$. The curves for $\epsilon = 10^{-5}$, $\epsilon = 10^{-6}$ and $\epsilon = 10^{-7}$ exhibit close agreement. The curves for $\epsilon = 10^{-3}$ and $\epsilon = 10^{-4}$ deviate from the curves for smaller values of ϵ, with $\epsilon = 10^{-4}$ showing better agreement than $\epsilon = 10^{-3}$, indicating convergence of D_{xy} as $\epsilon \to 0$. Similar results were obtained for other values of V, E_b, Ca and Δt as well as for other initial capsule geometries.

6.2. **Time Step Selection.** Because Δt is no longer linked to the spatial discretization, selection of the time step can be determined based on the desired accuracy of the simulation. In Figure 5(b) the deformation parameter is plotted for various values of the dimensionless time step, $k\Delta t$, along with the deformation parameter from the standard MRT LBM for simulations of an initially spherical capsule with Ca = 0.05, $V = 1$, $E_b = 0$, and $k = 2 \times 10^{-4}$ s^{-1}. For the multigrid LBM simulations a tolerance of $\epsilon = 10^{-5}$ was used.

From the figure it's clear that while $k\Delta t = 0.2$ captures the qualitative behavior of the deformation, the time step is too large to accurately resolve the dynamics. $k\Delta t = 0.1$, $k\Delta t = 0.02$ and $k\Delta t = 0.002$, however, all closely follow the deformation curve of the standard LBM simulation, with convergence to the standard LBM method as $k\Delta t \to k\delta t = 2 \times 10^{-5}$. From the inset to Figure 5(b) it can be seen that the curves for $k\Delta t = 0.002$ and $k\Delta t = 0.02$ fall on top of each other, with only a slight deviation from the deformation obtained from the standard LBM model, while the curve for $k\Delta t = 0.1$ shows slightly larger deviations from the standard LBM curve. Similar results are also found for larger values of Ca.

For a fixed value of k, the elastic time scale, $\tau_e = \text{Ca} \cdot k^{-1}$, is proportional to Ca. To account for this we set $k\Delta t = 0.02$ for Ca ≥ 0.05, while for Ca< 0.05 the time step is decreased proportionally with the capillary number. This can be summarized by the following equation:

$$k\Delta t = \min\left(0.4 \cdot \text{Ca}, 0.02\right). \tag{43}$$

In our simulations Equation (43) has been found to be sufficient for stable simulations for other values of k, E_b, V, and Ca, as well as for other capsule geometries.

7. Capsule Simulations

7.1. **Numerical Setup.** For the simulations presented here a mesh consisting of 2562 Lagrangian nodes, comprising 5120 triangular elements was used. The capsule is placed in the center of the fluid domain with its major axis aligned $\pi/4$ radians above the x-axis. The Eulerian grid is discretized into a 129^3 grid, with a domain of $[0, 12.8a]$ in x, y and z, which results in a step size of $\Delta x = \Delta y = \Delta z = 0.1a$. The simulations below are conducted with a Reynolds number of Re = 0.05, a capsule radius of $a = 1$ m, a density of $\rho = 1$ kg $\cdot$ m^{-3}, and a shear rate of $k = 2 \times 10^{-4}$ s^{-1}.

The simulations presented here were conducted with the time step, Δt, selected using Equation (43). The convergence criterion for the multigrid LBM was set to $\epsilon = 10^{-5}$ based on the results from Section 6. Each multigrid cycle uses a 5 grid level w-cycle multigrid schedule. The finest grid has a resolution of 129^3 and the coarsest grid has a resolution of 5^3.

The MRT relaxation parameters s_4 and s_1 are set according to Equations (15) and (16) respectively. The parameters s_0, s_3, s_5, and s_7 correspond to the conserved moments and are thus set equal to zero. The remaining relaxation parameters are set equal to 1.8.

The deformation parameter and inclination angle are computed using the method discussed in [12, 21]. First, we compute the capsule's moment of inertia:

$$I_{ij} = \int_V (r_k r_k \delta_{ij} - r_i r_j) dV, \tag{44}$$

where $\mathbf{r}$ is the radial vector, pointing outward from the capsule center. Both D_{xy} and θ are then obtained from the eigenvalues and eigenvectors of I. The eigenvalues of I correspond to the lengths of the axis of an ellipsoid with moment of inertia I. The lengths of the major and minor axis for this ellipsoid are used to approximate L and ℓ in Equation (5) [21]. The inclination angle, θ, is computed by finding the principle value of the angle between the capsule's major axis and the x axis.

7.2. **Spherical capsules.** The dynamics of spherical capsules in shear flow have been studied theoretically [5, 6] and numerically (e.g. [12, 14, 21, 22, 30]) and are well-known. Initially, the flow results in deformation of the sphere until the capsule reaches an ellipsoidal equilibrium shape. After reaching an equilibrium shape, the ambient shear flow causes the membrane to rotate about the internal fluid. This phenomenon, known as tank-treading, has also been observed experimentally for spherical [40] and biconcave [1] capsules.

In Figure 6 the results for simulations of initially spherical capsules are given for a variety of capillary numbers, Ca. Figures 6(a) and 6(b) plot the deformation parameter and inclination angle of the capsule as a function of time. The results are compared to the published results in [12] and [22] showing close agreement. As can be seen in the figures, the flow causes the sphere to gradually deform and rotate toward the x-axis. This process occurs until the capsule obtains a steady shape and inclination, as can be seen by the constant values of D_{xy} and θ/π for later values of the simulation. Increased values of Ca result in greater deformation and more rotation.

Figure 7(a) shows the final shapes obtained from our simulations as a function of the capillary number. As can be seen the final shapes move farther away from a sphere as Ca is increased. In Figure 7(b) the trajectory of a particle on the membrane surface is tracked for a capillary number of Ca=0.05. As can be seen, once the capsule reaches its final shape the particle rotates around the capsule in the tank-tread motion discussed above.

In Figure 8(a) the evolution of D_{xy} is plotted for initially spherical capsules with varying values of the dimensionless bending modulus, E_b. The capillary number is fixed at Ca=0.05, the viscosity ratio is fixed at $V = 1$, the spontaneous curvature is set at $c_0 = 0$. The capsules exhibit the same tank-treading behavior discussed above with close agreement between results from the present study and the results

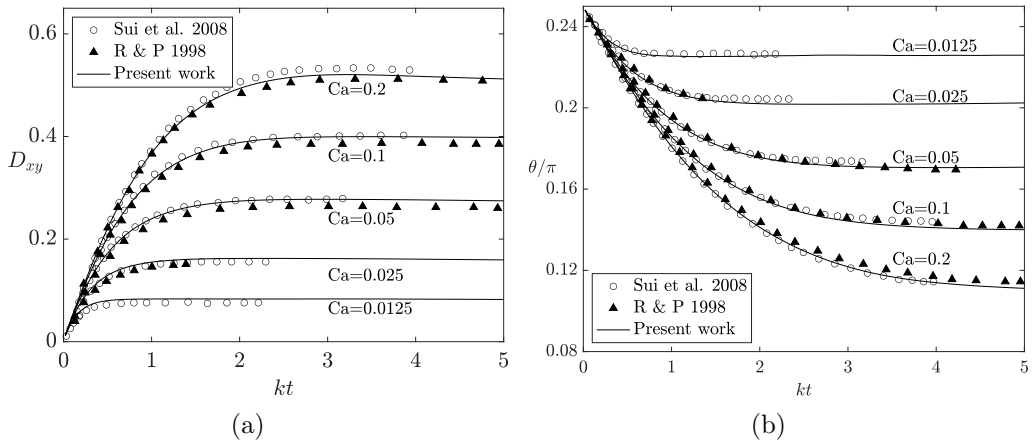

FIGURE 6. (a) The deformation parameter and (b) inclination angle for various values of Ca with $V = 1$ and $E_b = 0$.

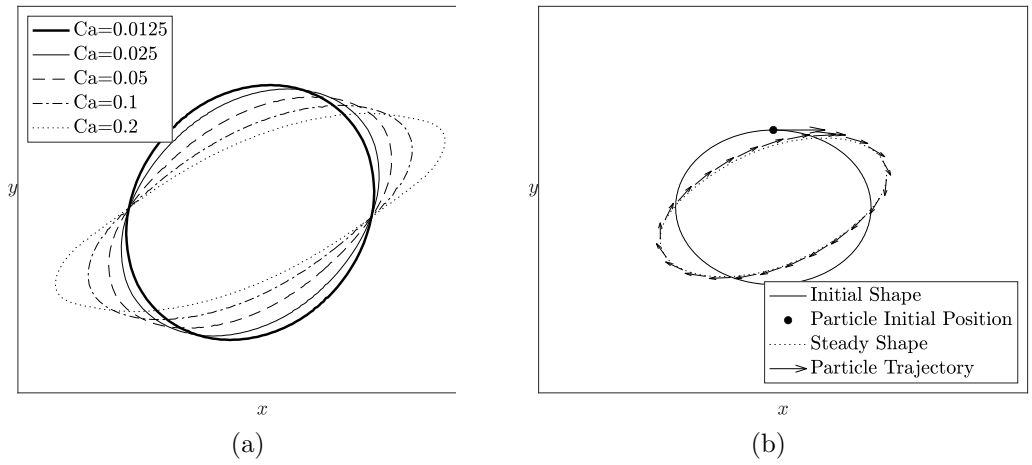

FIGURE 7. (a) Steady state shape of capsules for various values of Ca. (b) The trajectory of a particle for an initially spherical capsule with Ca=0.05.

published by Le in [42]. For a fixed capillary number, increasing E_b results in reduced deformation.

In Figure 9(a) the internal to external viscosity ratio is set to $V = 5$ for varying values of the capillary number. The effects of the membrane's bending stiffness are ignored by setting $E_b = 0$. Close agreement can be seen between the present results and those published by Le and Tan in [25] and Ramanujan and Pozrikidis in [12]. The capsules exhibit tank-treading behavior, however the increased viscosity ratio results in reduced deformation of the capsule when compared with the deformation seen for $V = 1$.

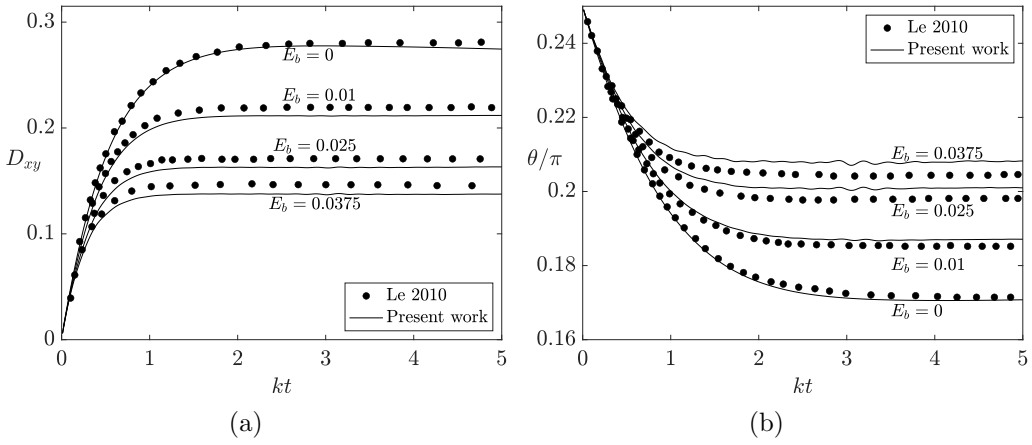

(a) (b)

FIGURE 8. (a) The deformation parameter and (b) inclination angle for initially spherical capsules with $Ca = 0.05$ and $V = 1$ for various values of E_b.

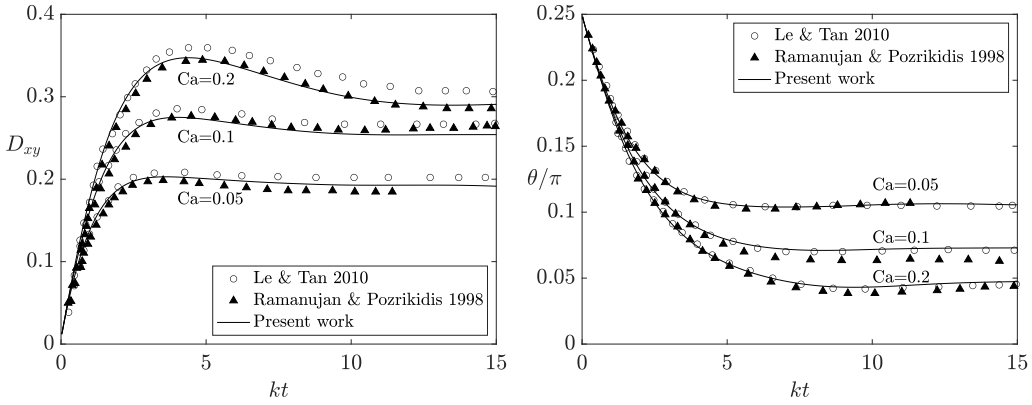

(a) (b)

FIGURE 9. (a) The deformation parameter and (b) inclination angle for initially spherical capsules $V = 5$ and $E_b = 0$ for various values of Ca.

In order to assess the range of validity for the quasi-steady approach proposed here, Figure 10 compares D_{xy} and θ/π for Re=0.05, Re=0.1, and Re=0.25 using the standard LBM, which solves the time-dependent incompressible Navier-Stokes equations, and the quasi-steady approach proposed here. In this figure the thin lines are the deformation parameter and the bold face lines are the inclination angle. Both simulations are conducted for spherical capsules with Ca = 0.05, $V = 1$, and $E_b = 0$ for a Neo-Hookean membrane. In Figure 10(a), for Re=0.05, the two numerical schemes are seen to produce nearly equivalent results, suggesting

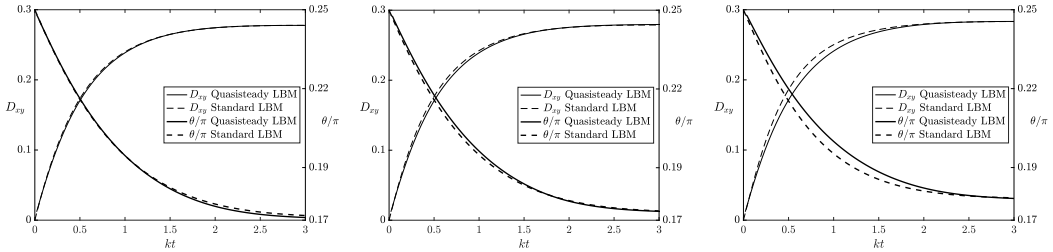

(a) (b) (c)

FIGURE 10. (a) The deformation parameter and inclination angle for (a) Re = 0.05, (b) Re = 0.1, and (c) Re = 0.25.

that for Re=0.05 neglecting the transient term of the Navier-Stokes equations does not affect the dynamics of the capsule deformation. In Figures 10(b) and 10(c), the deformation parameter and inclination angles are seen to reach the same equilibrium values for both fluid solvers, which is unsurprising since the capsule's attainment of an equilibrium shape results in a steady flow pattern. Before reaching the equilibrium shape, however, the deformation and inclination of the quasi-steady simulation can be seen to deviate from the standard LBM, with larger deviations occurring for the case with the larger Reynolds number, Re = 0.25. Based on these results, care should be taken when simulating the dynamics of phenomena with Re $\geq$ 0.1, as neglecting the transient term in the Navier-Stokes equations may affect the dynamics.

7.3. **Spheroid capsules.** To further demonstrate the efficacy of our method we consider the deformation of an oblate spheroid in shear flow. An oblate spheroid resembles a flattened sphere, with two axes of equal length and the length of the third axis less than that of the other two. The parametrization for an oblate spheroid can be given in terms of the azimuthal angle, ϕ, and polar angle, θ, as follows:

$$x = R\sin\theta\cos\phi \qquad z = R\sin\theta\sin\phi \qquad y = R\frac{b}{a}\cos\theta. \tag{45}$$

In Equation (45) R is used to adjust the radius so that the spheroid has a volume equivalent to the volume of a sphere with radius 1.

Unlike initially spherical capsules, the spheroids do not reach a constant steady shape. Instead, the capsule's shape and inclination oscillate while the membrane rotates around the interior fluid. For small enough values of Ca, the capsule's motion will transition from tank-treading to a tumbling motion [9, 58, 59].

In Figure 11 D_{xy} and θ/π are shown for a spheroid with $b/a = 0.9$ for $V = 1$, $E_b = 0$ and capillary numbers, Ca=0.05, Ca=0.1 and Ca=0.2. These simulations have been conducted by a number of authors including [12, 22, 42, 25, 27] Here,

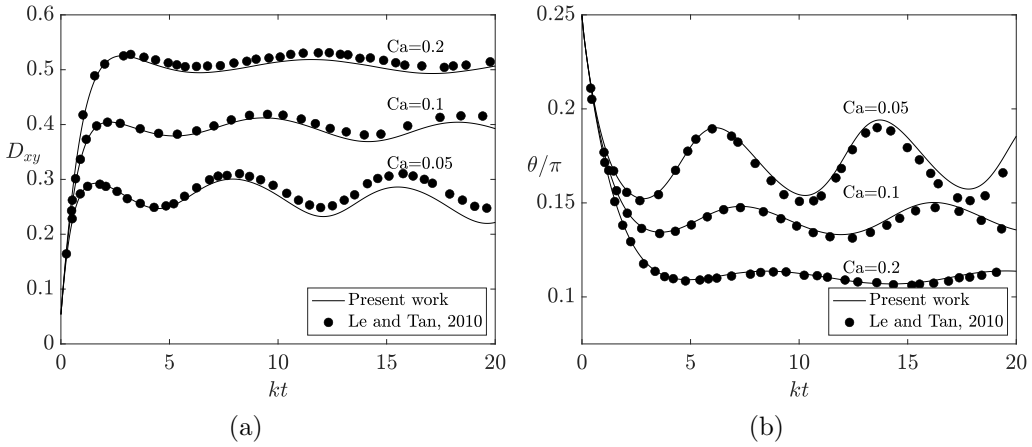

FIGURE 11. (a) The deformation parameter and (b) inclination angle for various values of Ca for a spheroid with $b/a = 0.9$.

the results are plotted alongside those reported by Le and Tan in [25]. Close agreement is observed between the present simulations and those in [25].

In Figure 12 D_{xy} and θ/π are shown for a spheroid with $b/a = 0.5$ for $V = 1$, $E_b = 0$ and capillary numbers, Ca=0.05, Ca=0.1 and Ca=0.2. For Ca=0.2 the results are compared with those reported by Sui et al. in [22], with close agreement seen between the two studies. For Ca=0.05 and Ca=0.1 Figure 12 provides a comparison between D_{xy} and θ/π for two fluid solvers: the quasi-steady method proposed in this work and the standard MRT lattice Boltzmann method. As can be seen in the figures, the results using the two fluid solvers are indistinguishable. This finding was true for all of the simulations presented in the present study, further suggesting that the quasi-steady approach is valid for Re = 0.05.

In Figures 13(a) and 13(b) the trajectory of a sinlge Lagrangian node on the capsule membrane is plotted for a simulation up to $kt = 20$ with Ca=0.05, $V = 1$ and $E_b = 0$ for spheroids with $b/a = 0.9$ and $b/a = 0.5$ respectively. Each arrow represents the particles current velocity for the duration of the simulation. The particle completes more than rotation around the capsule membrane during the simulation, illustrating the deviations in capsule shape for spheroid capsules. In Figure 13(a), the capsule with $b/a = 0.9$, undergoes, slight changes in the shape as the particle revolves around the interior fluid. In Figure 13(b) the capsule's shape and inclination angle oscillate more dramatically during tank treading. The larger deviations seen in Figure 13(b) are due to the larger difference between the major and minor axis of the spheroid, indicated by the lower value of b/a.

7.4. **Biconcave capsules.** Next we consider the deformation of an initially biconcave capsule in shear flow. The parametrization for a biconcave capsule used

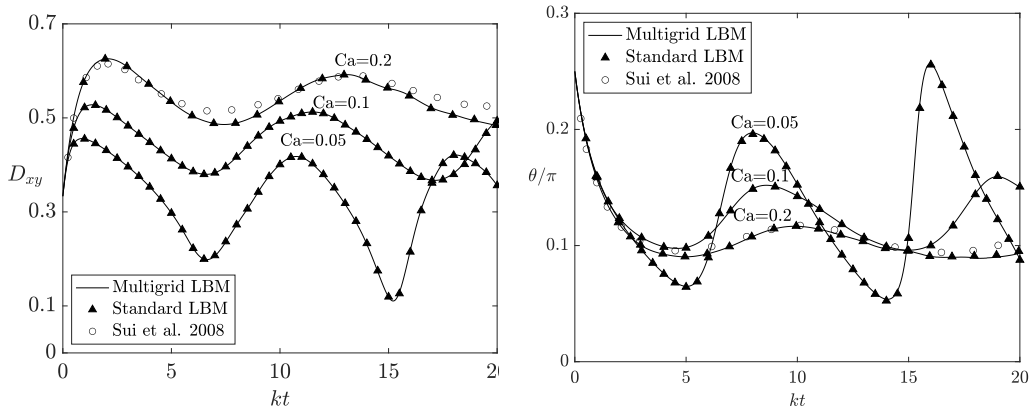

(a) (b)

FIGURE 12. (a) The deformation parameter and (b) inclination angle for various values of Ca for a spheroid with $b/a = 0.5$.

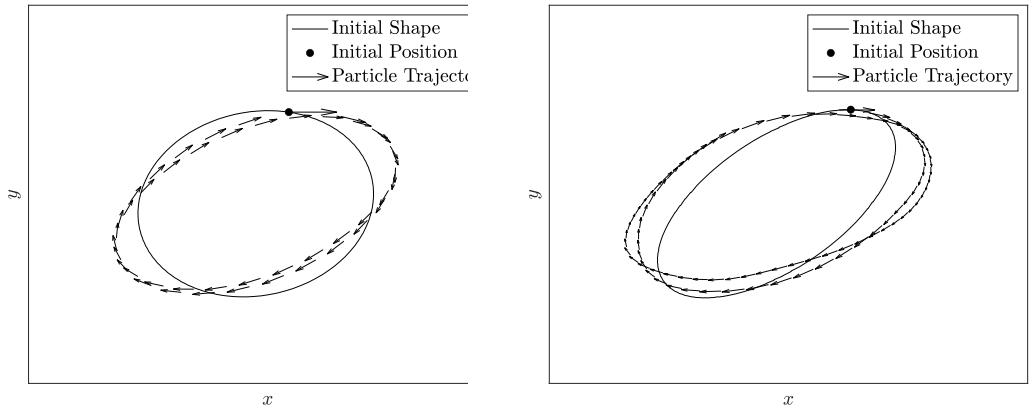

(a) (b)

FIGURE 13. (a) The trajectory of a particle on an initially spheroidal capsule with b/a=0.9 with Ca=0.05. (b) The trajectory of a particle on an initially spheroidal capsule with b/a=0.5 with Ca=0.05.

here is given by Fung in [60] as:

$$x = a\alpha\sin\theta\cos\phi \quad y = \frac{a\alpha}{2}(k_0 + k_1\sin^2\theta - k_2\sin^4\theta)cos\theta \quad z = a\alpha\sin\theta\sin\phi \tag{46}$$

where $\alpha = 1.3858$, $k_0 = 0.207$, $k_1 = 2.003$, and $k_2 = 1.123$, and a is the radius of a sphere with the same volume as the capsule. The resulting mesh can be seen in Figure 3(b).

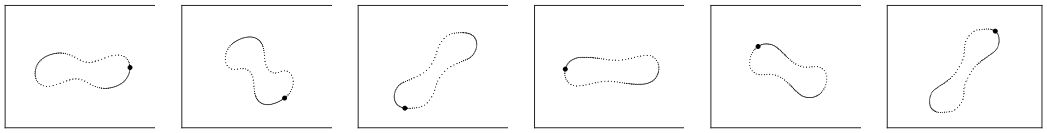

(a) (b) (c) (d) (e) (f)

FIGURE 14. The profile of an initially biconcave capsule at (a) $kt = 5$, (b) $kt = 8$, (c) $kt = 11$, (d) $kt = 15$, (e) $kt = 18$, and (f) $kt = 21$. The black dot is the location of a marker point on the membrane.

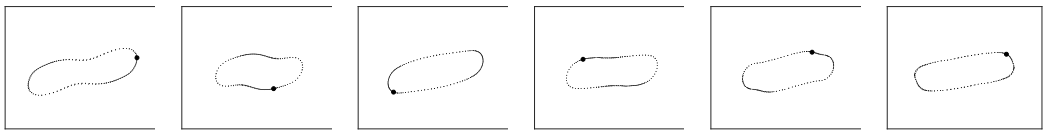

(a) (b) (c) (d) (e) (f)

FIGURE 15. The profile of an initially biconcave capsule at (a) $kt = 4$, (b) $kt = 10$, (c) $kt = 16$, (d) $kt = 22$, (e) $kt = 28$, and (f) $kt = 30$. The black dot is the location of a marker point on the membrane.

A variety of values of the spontaneous curvature, c_0, can be found in the literature. In [26, 61] a constant negative value is used for the spontaneous curvature. We have followed [20, 62] and set the spontaneous curvature, c_0, in Equation (31) to $c_0 = -2H_0$, where H_0 is the initial curvature of the capsule. This selection of the spontaneous curvature facilitates comparison between the present work and [20, 62].

Although [20] and [62] used the same spontaneous curvature, they chose different values for E_b. In this work we use the values reported by Sinha and Graham in [20], which are $E_b = 0.03$ and $C = 10$. The surface elasticity modulus, G_s, used in [20] corresponds to $E_s = 2G_s$, requiring us to re-scale these quantities by 1/2. Thus, in this work, the bending stiffness was held fixed at $E_b = 0.015$ and Skalak's strain energy functional was used with a value of $C = 5$, matching the values used in [20].

The dynamics of biconcave capsules in shear flow can be broadly grouped into two categories: a tumbling phase and a tank-treading phase. The tumbling phase typically occurs at low shear rates and high viscosity ratios. In the tumbling phase the capsule's shape remains roughly constant while the capsule undergoes rotations in the plane of shearing. Figure 14 shows the profile of an initially biconcave capsule with $E_b = 0.015$, Ca=0.25, and $V = 4$ undergoing the tumbling motion. As can be seen in the figure, the capsule retains the biconcave shape while rotating around in the center of the domain.

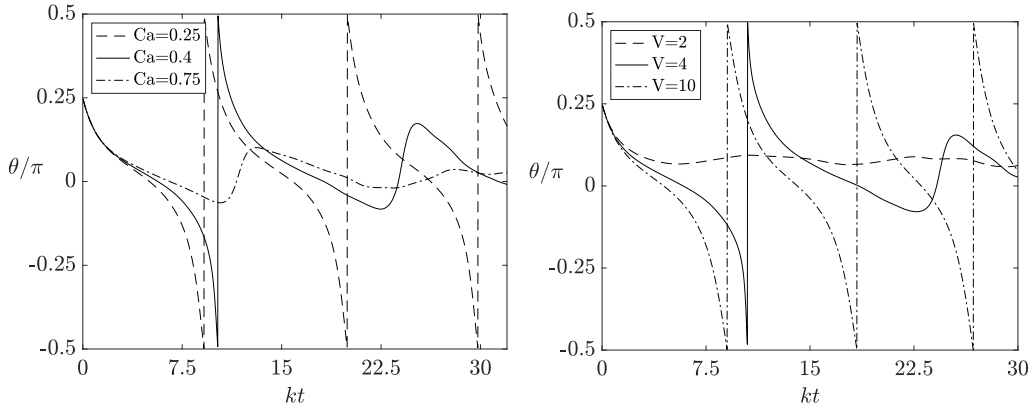

(a) (b)

FIGURE 16. (a) The inclination angle for capsules with various dimensionless shear rates. (b) The inclination angle for capsules with various viscosity ratios.

The tank-treading phase, which typically occurs at higher shear rates and lower viscosity ratios, is characterized by a rotation of the capsule membrane around the interior fluid. Figure 15 shows the profile of an initially biconcave capsule with $E_b = 0.015$, Ca=0.75, and $V = 4$ undergoing the tank-treading motion. As can be seen, the shape and inclination angle remain roughly constant throughout the motion, while the membrane rotates around the interior fluid. In between these two phases are transition phases, where a capsule will oscillate between these two behaviors or exhibit more complicated dynamics that combine the two motions [18, 20, 26, 28].

Figure 16 shows the inclincation angle for biconcave capsules in shear flow with $E_b = 0.015$, $C = 5$ and spontaneous curvature $c_0 = -2H_0$. Figure 16(a) illustrates the effect of increased capillary numbers. The viscosity ratio for the simulations in Figure 16(a) was $V = 4$. At Ca=0.25 the capsule undergoes tumbling motion. At Ca=0.4 the capsule first begins a tumbling motion, rotating π radians before reaching a roughly constant inclination angle with a tank-treading motion. At Ca=0.75 the capsule undergoes tank-treading motion.

Figure 16(b) illustrates the effect of increasing the viscosity ratio. The capillary number for the simulations in Figure 16(b) are Ca=0.4. At $V = 2$ the capsule undergoes tank-treading motion, at $V = 4$ the capsule is in a transition phase, and at $V = 10$ the capsule undergoes tumbling motion. As can be seen, increasing the viscosity ratio has a similar effect to decreasing the capillary number.

A number of numerical [26, 62, 61, 20] and experimental [4] studies have been conducted on the motion of red blood cells as a function of the capillary number and viscosity ratio. In order to assess the fidelity of our model we ran simulations with viscosity ratios ranging from $V = 0.5$ to $V = 10$ and capillary numbers ranging

from Ca=0.05 to Ca=1. The simulations were then categorized as undergoing a tank-treading phase, a tumbling phase or a transitional phase.

The results from these simulations can be seen in Figure 17. The plot also includes the boundaries between the tank-treading and tumbling phases found by Sinha and Graham in [20] and Le and Tan in [62]. The boundaries between the different phases of motion exhibit close qualitative and quantitative agreement.

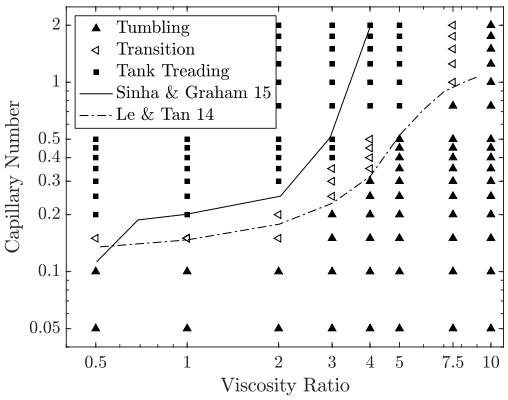

FIGURE 17. Classification of simulations with biconcave capsules for a variety of capillary numbers and viscosity ratios.

8. Computational Efficiency

To demonstrate the efficiency gains attained with the dual-time stepping strategy proposed in this work, we have conducted simulations for spherical and biconcave capsules for a variety of dimensionless parameters using the standard LBM-IBM capsule model and the DTS method proposed in this work. The simulations were run on the Turing High Performance Computing Cluster at Old Dominion University using 2.3 GHz CPUs with 128 GB RAM. The resolution on the fine grid was $N = 129$ in each dimension for both the single grid and multigrid simulations. The Eulerian domain used was $[0, 12.8a]^3$ for both simulations which, coupled with the resolution of $N = 129$ in each direction, results in a time step of $\delta t = 0.1a$ s for the standard LBM simulation. As in Section 7, the simulations in this section are normalized by setting Re=0.05, $a = 1$ m, and $\rho = 1$ kg $\cdot$ m^{-3}. The capsule mesh consists of 5120 triangular elements comprised of 2562 Lagrangian nodes. For the DTS scheme the time step was chosen using Equation (43) and an iterative tolerance of $\epsilon = 10^{-5}$ was used.

8.1. **Efficiency for Spherical Simulations.** To study the speed-up offered by the newly proposed method we conduct simulations for spherical capsules using the standard LBM-IBM capsule model and the DTS scheme proposed here. The capsules were assumed to have Neo-Hookean membranes with $V = 1$ and $E_b =$

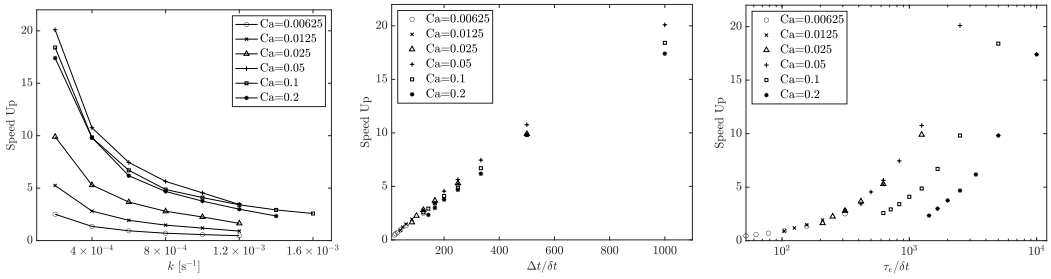

FIGURE 18. (a) The speed-up as a function of the shear rate, k. (b) The speed-up as a function of the ratio $\Delta t/\delta t$. (c) The speed-up as a function of the ratio $\tau_e/\delta t$.

0 with capillary numbers ranging from 0.00625 to 0.2 and shear rates ranging from 2×10^{-4} s^{-1} to 1.6×10^{-3} s^{-1}. To facilitate comparison across capillary numbers, we alter the duration of the simulations based on the capillary number. For simulations with Ca = 0.00625 the simulations are run up to $kT = 0.5$, for Ca = 0.0125 simulations are run up to $kT = 1$, for Ca = 0.025 simulations are run up to $kT = 2$, and for Ca $\geq$ 0.05 we simulate up to $kT = 4$. This accounts for the smaller elastic time scales and smaller values of $k\Delta t$ used at smaller values of Ca.

In Figure 18(a) the speed-up achieved by the DTS method is plotted against the shear rate. As can be seen in the figure, the speed-up offered by the DTS method is proportional to Ca and inversely proportional to k. Both of these relationships can be understood by examining the time step constraint for the DTS scheme given by Equation (43). The dimensionless time step for the standard LBM, $k\delta t$, is determined by k for a fixed value of Ca, whereas for the DTS scheme the dimensionless physical time step, $k\Delta t$, varies with Ca for a fixed value of k.

The size of the physical time step, Δt, is a strong predictor of the potential speed-up obtained by the DTS scheme. This relationship can be seen in Figure 18(b), which plots the speed-up against the ratio $\Delta t/\delta t$. As can be seen in the figure, when $\Delta t/\delta t = 100$ a speed-up of 2 is achieved with the DTS scheme. The speed-up increases proportionally as $\Delta t/\delta t$ increases, with peak efficiencies on the order of 20 for larger values of Ca. Based on this, the physical time scale and accuracy of the scheme should allow for increases of the physical time step by a factor of 100 or more for efficient application of the DTS scheme proposed here.

To demonstrate the limiting effects of the physical time scales and the accuracy requirements we have plotted the speed-up achieved by the DTS method against the ratio, $\tau_e/\delta t$ using a logarithmic scale for the x axis in Figure 18(c). The ratio $\tau_e/\delta t$ indicates the separation of scale between the physical time scales and the LBM time step. From Equation (43) we see that for Ca $\leq$ 0.05 Δt is limited by the elastic time scale of the problem, whereas for Ca = 0.1 and Ca = 0.2 the

time step is limited by the desired accuracy of the simulation. This relationship is apparent in the figure, where the speed-up curves for Ca $\leq$ 0.05 are nearly identical, while Ca = 0.1 and Ca = 0.2 have distinct speed-up curves. From the figure we recommend that $\tau_e/\delta t$ be on the order of 200 or more for efficient implementation of the DTS scheme proposed here.

While the speed-up achieved using the DTS scheme diminishes as k increases, for long simulations and non-spherical geometries k is limited by the stability constraint in Equation (39). Indeed, even for the spherical simulations discussed here $k > 1.2 \times 10^{-3}$ s^{-1} resulted in instability for some values of Ca. It should also be mentioned that, since small values of Ca reach equilibrium in a shorter time frame, declines in efficiency with the DTS scheme for small values of Ca are not a major concern because the standard LBM-IBM capsule model can simulate these in a reasonable amount of time. The most dramatic speed-up from the DTS scheme occur for Ca $\geq$ 0.0125 where simulation with the standard LBM-IBM capsule model can be much more expensive. In this regime, speed-up between 4 and 20 times the standard LBM-IBM capsule model are achieved.

8.2. **Efficiency for Biconcave Simulations.** Simulating the dynamics of non-spherical capsules require much longer simulations because the capsules do not reach an equilibrium shape or flow field. These long simulations place more stringent constraints on the shear rate k, increasing the potential speed-up offered by the DTS scheme. We find that $k \leq 2 \times 10^{-4}$ s^{-1} is required for simulations long enough to capture the dynamics of biconcave capsules. For the standard LBM-IBM capsule model this results in a dimensionless time step of $k\delta t = 2 \times 10^{-5}$, which is far below the time step of the DTS scheme, which is set to $k\Delta t = 0.02$ for the simulations in this section.

To study the efficiency gains for capsule simulations where the flow does not reach a steady state, we have run simulations with a biconcave capsule for each of the cases illustrated in Figure 16(a). As in the figure, the viscosity ratio was set to $V = 4$, the bending stiffness was set to $E_b = 0.015$, and Skalak's modulus was set to $C = 5$. Simulations were run up to $kt = 30$ for Ca=0.25, Ca=0.4 and Ca=0.75. These three cases were chosen to demonstrate the effect that the different capsule behaviors has on the computational efficiency of the model, as Ca=0.25 results in a tumbling capsule, Ca=0.4 results in a transient regime, and Ca=0.75 results in a tank-treading capsule.

TABLE 1. CPU time comparison for a biconcave capsule with $V = 4$ and $E_b = 0.015$ for the cases shown in Figure 16(a) run until $kt = 30$

	Ca=0.25		Ca=0.4		Ca=0.75	
	LBM	mgLBM	LBM	mgLBM	LBM	mgLBM
Time (s)	322,339	43,693	322,373	16,661	322,423	9147
Efficiency	1.0	7.4	1.0	19.3	1.0	35.2

The results for these tests can be seen in Table 1. As can be seen, the efficiency gains of the simulation improve as the capillary number increases. It should be noted that unlike the spherical case above, the relationship between Ca and CPU time is not related to Δt. As mentioned above, $k\Delta t = 0.02$ for each value of Ca considered here. Instead the relationship between Ca and CPU time is due to the behavior of the capsule at the various capillary numbers as illustrated in Figure 16(a).

In the tumbling regime at Ca=0.25, the position of the capsule within the fluid changes at each time step. This alters the flow field near the capsule, requiring more iterations of the multigrid LBM algorithm at each time step. In the transient regime at Ca=0.4, the capsule begins by tumbling before oscillating slightly around $\theta = 0$ with minimal deformation. Thus, after the tumbling phase is completed and changes in the capsule's inclination angle are reduced, variations in the flow field decrease allowing faster convergence with the multigrid LBM at each time step. Finally, in the tank-treading regime at Ca=0.75, the capsule's angle remains roughly constant as the membrane rotates around the capsule. Thus, after reaching the steady shape, variation in the flow field is reduced between time steps, requiring fewer iterations of the fluid solver at each time step.

9. Discussion

In this work a quasi-steady, dual time-stepping lattice Boltzmann method was presented for flow-induced capsule deformation simulations using the Immersed Boundary Method. The method was validated by comparing the results to those reported in previous studies for a wide range of dimensionless parameters and capsule geometries. Separating the LBM time step from the capsule time step results in simulations on the order of 10 times faster than those achieved by the standard LBM-IBM capsule model. Furthermore, de-coupling the physical time step from the LBM time step allows us to choose the physical time step based on the stability constraints of the elastic problem, without consideration for the LBM scheme.

The proposed method treats the flow as a quasi-steady problem and thus the method is limited to flows in the low Reynolds number regime. In order to ensure physical fidelity, careful consideration of the expected dynamics is required when using this numerical scheme for $\mathrm{Re} \geq 0.1$. For phenomena where the quasi-steady assumption does not hold, the method proposed by Gsell et al. in [38] could be employed. In the low Reynolds number regime discussed in this work, the proposed method has some advantages over the method from [38]. Neglecting the transient term reduces the memory footprint of the algorithm by avoiding storage of the previous velocity and density fields. The present method also employs the standard LBM procedures for the collision and streaming steps, allowing for quick implementation into current LBM-IBM capsule codes.

For efficient application of the DTS scheme the physical time step should be several orders of magnitude larger than the tradition LBM time step in order to defray the additional computational cost per time step. We find that the DTS scheme is twice as fast as the LBM scheme when a physical time step 100 times larger than the LBM time step is used. Larger differences between the two time steps increase the speed-up of the DTS scheme proportionally. For a given application the suitability of the proposed scheme is related to the ratio of the physical time scale to the LBM time step. For elastic capsule simulations the minimum ratio of $\tau_e/\delta t$ for a speed-up of 2 using the DTS scheme is approximately 200.

For the parameter regime in which standard LBM-IBM models of capsule deformation are most computationally expensive, the DTS scheme presented in this work results in speed-up on the order of 20. Even for parameter regimes in which the increasing the physical time step is limited by the separation of scales we find speed-up on the order of 4-10 times the standard LBM-IBM capsule. Future directions could include the consideration of additional membrane forces such as those arising from the membrane's viscosity or those exerted on the membrane by an electrostatic field. The development of a more efficient iterative solver or a refined residual equation could also offer potential improvements to the fluid algorithm presented in this work.

10. Acknowledgements

Support from National Science Foundation grant DMS-1319078 is gratefully acknowledged. This research was supported by the Turing High Performance Computing cluster at Old Dominion University.

References

[1] H. Schmid-Schönbein and R. Wells, "Fluid drop-like transition of erythrocytes under shear," *Science*, vol. 165, pp. 3288–291, 1969.

[2] H. Goldsmith and J. Marlow, "Flow behaviour of erythrocytes i: Rotation and deformation in dilute suspensions," *Proceedings of the Royal Society London B*, vol. 182, pp. 351–384, 1972.

[3] J. Dupire, M. Socol, and A. Viallat, "Full dynamics of a red blood cell in shear flow," *Proceedings of the National Academy of Sciences for the United States of America*, vol. 109(51), pp. 20808–20813, 2012.

[4] T. Fischer and R. Korzeniewski, "Threshold shear stress for the transition between tumbling and tank-treading of red blood cells in shear flow: dependence on the viscosity of the suspending medium," *Journal of Fluid Mechanics*, vol. 736, pp. 351–365, 2013.

[5] D. Barthés-Biesel, "Motion of a spherical microcapsule freely suspended in a linear shear flow," *Journal of Fluid Mechanics*, vol. 100, pp. 831–853, 1980.

[6] D. Barthés-Biesel and J. Rallison, "The time-dependent deformation of a capsule freely suspended in a linear shear flow," *Journal of Fluid Mechanics*, vol. 113, pp. 251–267, 1981.

[7] S. Keller and R. Skalak, "Motion of a tank-treading ellipsoidal particle in shear flow," *Journal of Fluid Mechanics*, vol. 120, pp. 27–47, 1982.

[8] J. Skotheim and T. Secomb, "Red blood cells and other nonspherical capsules in shear flow: oscillatory dynamics and the tank-treading-to-tumbling transition," *Physical Review Letters*, vol. 98, p. 078301, 2007.
[9] M. Abkarian, M. Faivre, and A. Viallat, "Swinging of red blood cells under shear flow," *Physical Review Letters*, vol. 98, p. 188302, 2007.
[10] C. Pozrikidis, "Finite deformation of liquid capsules enclosed by elastic membranes in simple shear flow," *Journal of Fluid Mechanics*, vol. 297, pp. 123–152, 1995.
[11] C. Pozrikidis, "Effect of membrane bending stiffness on the deformation of capsules in simple shear flow," *Journal of Fluid Mechanics*, vol. 440, pp. 2669–2691, 2001.
[12] S. Ramanujan and C. Pozrikidis, "Deformation of liquid capsules enclosed by elastic membranes in simple shear flow: Large deformations and the effect of fluid viscosities," *Journal of Fluid Mechanics*, vol. 361, pp. 117–143, 1998.
[13] C. Peskin, "The immersed boundary method," *Acta Numerica*, vol. 11, pp. 479–517, 2002.
[14] C. Eggleton and A. Popel., "Large deformation of red blood cell ghosts in a simple shear flow," *Physics of Fluids*, vol. 10, pp. 1834–1845, 1998.
[15] T. Omomori, T. Ishikawa, D. Barthés-Biesel, A.-V. Salsac, Y. Imai, and T. Yamaguchi, "Tension of red blood cell membrane in simple shear flow," *Physical Review E*, vol. 86, p. 056321, 2012.
[16] A. Farutin, T. Biben, and C. Misbah, "3d numerical simulations of vesicle and inextensible capsule dynamics," *Journal of Computational Physics*, vol. 275, pp. 539–568, 2014.
[17] Z. Peng, A. Mashayekh, and Q. Zhu, "Erythrocyte responses in low-shear-rate flows: effects of non biconcave stress-free state in the cytoskeleton," *Journal of Fluid Mechanics*, vol. 742, pp. 96–118, 2014.
[18] K. Tsubota, S. Wada, and H. Liu, "Elastic behavior of a red blood cell with the membranes nonuniform natural state: equilibrium shape, motion transition under shear flow, and elongation during tank-treading motion," *Biomechanical Modeling and Mechanobiology*, vol. 13, pp. 735–746, 2014.
[19] Z. Peng, S. Salehyar, and Q. Zhu, "Stability of the tank-treading modes of erythrocytes and its dependence on cytoskeleton reference states," *Journal of Fluid Mechanics*, vol. 771, pp. 449–467, 2015.
[20] K. Sinha and M. Graham, "Dynamics of a single red blood cell in simple shear flow," *Physical Review E*, vol. 92, p. 042710, 2015.
[21] X. Li and K. Sarkar, "Front tracking simulation of deformation and buckling instability of a liquid capsule enclosed by an elastic membrane," *Journal of Computational Physics*, vol. 227, pp. 4998–5018, 2008.
[22] Y. Sui, Y. Chew, P. Roy, and H. Low, "A hybrid method to study flow-induced deformation of three-dimensional capsules," *Journal of Computational Physics*, vol. 227, pp. 6351–6371, 2008.
[23] Y. Sui, Y. Chew, P. Roy, Y. Cheng, and H. Low, "Dynamic motion of red blood cells in simple shear flow," *Physics of Fluids*, vol. 20, p. 112106, 2008.
[24] D. Le, "Effect of bending stiffness on the deformation of liquid capsules enclosed by thin shells in shear flow," *Physical Review E*, vol. 82, p. 016318, 2017.
[25] D. Le and Z. Tan, "Large deformation of liquid capsules enclosed by thin shells immersed in the fluid," *Journal of Computational Physics*, vol. 229, pp. 4097–4116, 2010.
[26] A. Z. K. Yazdani and P. Bagchi, "Phase diagram and breathing dynamics of a single red blood cell and a biconcave capsule in dilute shear flow," *Physical Review E*, vol. 84, p. 026314, 2011.

[27] W. Huang, C. Chang, and H. Sung, "Three-dimensional simulation of elastic capsules in shear flow by the penalty immersed boundary method," *Journal of Computational Physics*, vol. 231, pp. 3340–3364, 2012.
[28] D. Cordasco and P. Bagchi, "Intermittency in red blood cell dynamics," *Journal of Fluid Mechanics*, vol. 759, pp. 472–488, 2014.
[29] D. Mavriplis, "Multigrid solution of the steady-state lattice boltzmann equation," *Computers & Fluids*, vol. 35, pp. 793–804, 2006.
[30] T. Krüger, F. Varnik, and D. Raabe, "Efficient and accurate simulations of deformable particles immersed in a fluid using a combined immersed boundary lattice boltzmann finite element method," *Computers and Mathematics with Applications*, vol. 61, pp. 3485–3505, 2011.
[31] J. Gounley and Y. Peng, "Response and recovery times of elastic and viscoelastic capsules in shear flow," *Communications in Computational Physics*, vol. 17(5), pp. 1151–1168, 2015.
[32] J. Charrier, S. Shrivastava, and R. Wu, "Free and constrained inflation of elastic membranes in relation to thermoforming - non-axisymmetric problems," *Journal of Strain Analysis*, vol. 24(2), pp. 55–74, 1989.
[33] W. Helfrich, "Elastic properties of lipid bilayers: theory and possible experiments," *Z. Naturforsch*, vol. 28, pp. 693–703, 1973.
[34] O. Zhong-can and W. Helfrich, "Bending energy of vesicle membranes: General expressions for the first, second, and third variation of the shape energy and applications to spheres and cylinders," *Physical Review A*, vol. 39(10), pp. 5280–5288, 1989.
[35] J. Zhang, P. C. Johnson, and A. S. Popel, "An immersed boundary lattice boltzmann approach to simulate deformable liquid capsules and its application to microscopic blood flows," *Physical Biology*, vol. 4, pp. 285–295, 2007.
[36] A. Ghaffarian and K. Hejranfar, "An implicit dual-time stepping pectral dfifference lattice boltzmann method for simulation of viscous compressible flows on structured meshes," *Meccanica*, vol. 54, pp. 1561–1581, 2019.
[37] G. Guzel and I. Koc, "Time-accurate flow simulations using a finite-volume based lattice boltzmann flow solver with dual time stepping scheme," *International Journal of Computational Methods*, vol. 13(6), p. 1650035, 2016.
[38] S. Gsell, U. D'Ortona, and J. Favier, "Multigrid dual-time stepping lattice boltzmann method," *Physical Review E*, vol. 101, p. 023309, 2020.
[39] K. Chang and W. Olbricht, "Experimental studies of the deformation and breakup of a synthetic capsule in steady and unsteady simple shear flow," *Journal of Fluid Mechanics*, vol. 250, pp. 609–633, 1993.
[40] A. Walter, H. Rehage, and H. Leonhard, "Shear induced deformation of microcapsules: shape oscillations and membrane folding," *Colloids and Surfaces A*, vol. 183-185, pp. 123–132, 2001.
[41] E. Lac, D. Barthés-Biesel, N. Pelekasis, and J. Tsamopoulos, "Spherical capsules in three-dimensional unbounded stokes flows: effect of the membrane constitutive law and onset of buckling," *Journal of Fluid Mechanics*, vol. 516, pp. 303–334, 2004.
[42] D. V. Le, "Subdivision elements for large deformation of liquid capsules enclosed by thin shells," *Computer Methods in Applied Mechanics and Engineering*, vol. 199, pp. 2622–2632, 2010.
[43] G. Taylor, "The formulation of emulsions in definable fields of flow," *Proceedings of the Royal Society*, vol. 146(858), pp. 501–523, 1934.
[44] D. d'Humiéres, I. Ginzburg, M. Krafczyk, P. Lallemand, and L. Luo, "Multiple-relaxation-time lattice boltzmann models in three dimensions," *Philosophical Transactions of The*

Royal Society A Mathematical Physical and Engineering Sciences, vol. 360, pp. 437–451, 2002.

[45] P. Lallemand, L. Luo, and Y. Peng, "A lattice boltzmann front-tracking method for interface dynamics with surface tension n two dimensions," *Journal of Computational Physics*, vol. 226(2), pp. 1367–1384, 2007.

[46] D. Patil, K. N. Premnath, and S. Banerjee, "Multigrid lattice boltzmann method for accelerated solution of elliptic equations," *Journal of Computational Physics*, vol. 265, pp. 172–194, 2014.

[47] R. Skalak, A. Tozeren, R. Zarda, and S. Chien, "Strain energy functions of red blood cell membranes," *Biophysical Journal*, vol. 13, pp. 245–264, 1973.

[48] D. Barthés-Biesel, A. Diaz, and E. Dhenin, "Effect of constitutive laws for two-dimensional membranes on flow-induced capsule deformation," *Journal of Fluid Mechanics*, vol. 460, pp. 211–222, 2002.

[49] A. Guckenberg, M. Schrame, P. G. Chen, M. Leonetti, and S. Gekle, "On the bending algorithms for soft objects in flows," *Computer Physics Communications*, vol. 207, pp. 1–23, 2016.

[50] A. Guckenberg and S. Gekle, "Theory and algorithms to compute helfrich bending forces: a review," *Journal of Physics: Condensed Matter*, vol. 29, p. 203001, 2017.

[51] R. Garimella and B. Swartz, "Curvature estimation for unstructured triangulations of surfaces," *Technical Report, LA-UR-03-8240*, 2003.

[52] M. Reuter, S. Biasotti, D. Giorgi, G. Patané, and M. Spagnuolo, "Discrete laplace-beltrami operators for shape analysis and segmentation," *Computer & Graphics*, vol. 33, pp. 381–390, 2009.

[53] U. Pinkall and K. Polthier, "Computing discrete minimal surfaces and their conjugates," *Experimental Mathematics*, vol. 2, pp. 15–36, 1993.

[54] J. Walter, A.-V. Salsac, D. Barthés-Biesel, and P. L. Tallec, "Coupling of finitel element and boundary integral methods for a capsule in a stokes flow," *International Journal for Numerical Methods in Engineering*, vol. 83, pp. 829–850, 2010.

[55] J. Walter, A.-V. Salsac, and D. Barthés-Biesel, "Ellipsoidal capsules in simple shear flow: prolate versus oblate initial shapes," *Journal of Fluid Mechanics*, vol. 676, pp. 318–347, 2011.

[56] D. Barthés-Biesel, "Motion and deformation of elastic capsules and vesicles in flow," *Annual Review of Fluid Mechanics*, vol. 48, pp. 25–52, 2016.

[57] C. Armstrong and Y. Peng, "An mrt extension to the multigrid lattice boltzmann method," *Communications in Computational Physics*, vol. 26(4), pp. 1178–1195, 2019.

[58] S. Kessler, R. Finken, and U. Seifert, "Swinging and tumbling of elastic capsules in shear flow," *Journal of Fluid Mechanics*, vol. 605, pp. 207–226, 2008.

[59] P. Bagchi and R. Kalluri, "Dynamics of nonspherical capsules in shear flow," *Physical Review E*, vol. 80, p. 016307, 2009.

[60] Y. Fung, *Biomechanics: Mechanical properties of living tissues*. Springer-Verlag, 1993.

[61] D. Cordasco, A. Yazdani, and P. Bagchi, "Comparison of erythrocyte dynamics in shear flow under different stress-free configurations," *Physics of Fluids*, vol. 26, p. 041902, 2014.

[62] D. Le and Z. Tan, "Hydrodynamic interaction of elastic capsules in bounded shear flow," *Communications in Computational Physics*, vol. 16(4), pp. 1031–1055, 2014.